Journal of Colloid and Interface Science 608 (2022) 2066–2074

Contents lists available at ScienceDirect

Journal of Colloid and Interface Science

journal homepage: www.elsevier.com/locate/jcis

Engineering cobalt nitride nanosheet arrays with rich nitrogen defects as a bifunctional robust oxygen electrocatalyst in rechargeable Zn–air batteries

Yan Hu[a,1], Man Guo[a,1], Chuan Hu[a], Jiaxin Dong[a,*], Puxuan Yan[a], Tayirjan Taylor Isimjan[b,*], Xiulin Yang[a,*]

[a] Guangxi Key Laboratory of Low Carbon Energy Materials, School of Chemistry and Pharmaceutical Sciences, Guangxi Normal University, Guilin 541004, China

[b] Saudi Arabia Basic Industries Corporation (SABIC) at King Abdullah University of Science and Technology (KAUST), Thuwal 23955-6900, Saudi Arabia

HIGHLIGHTS

- $CoN\text{-}N_d$ nanosheet with nitrogen defects was synthesized by solvothermal and nitridation treatment.
- The catalyst exhibits highly active OER/ORR performance than benchmark Pt/C.
- The catalyst displays a superb stability for 260 cycles superior to Pt/C in Zn-air battery.
- The nitrogen defect sites, high conductivity, and array-like structure dominate the superb performance.

GRAPHICAL ABSTRACT

The $CoN\text{-}N_d$ nanosheet with nitrogen defects was synthesized by solvothermal and low-temperature nitridation as a high-efficiency OER and ORR electrocatalyst for rechargeable Zn-air batteries. The excellent performance is attributed to the unique structure providing abundant active sites, faster charge transfer rate, electrolyte diffusion rate and gas release.

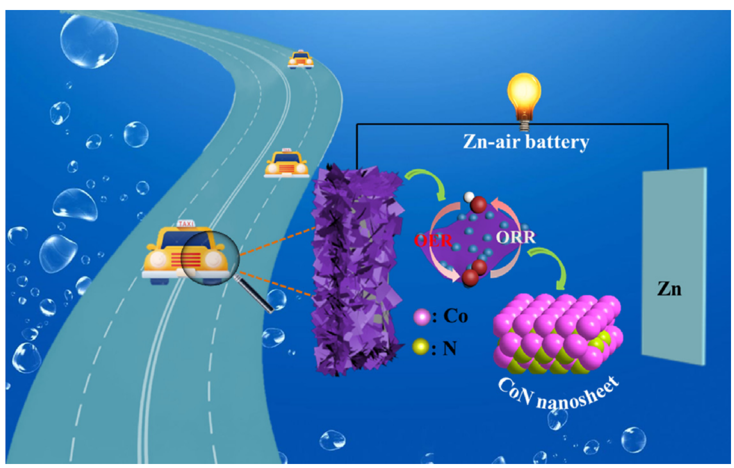

ARTICLE INFO

Article history:
Received 29 August 2021
Revised 20 October 2021
Accepted 22 October 2021
Available online 28 October 2021

Keywords:
CoN nanosheet
Defect
Oxygen evolution
Oxygen reduction
Zinc-air battery

ABSTRACT

Developing high-activity bifunctional oxygen electrocatalysts to overcome the sluggish $4e^-$ kinetics is an urgent challenge for rechargeable metal-air batteries. Here, we prepared a CoN nanosheet catalyst with rich nitrogen defects ($CoN\text{-}N_d$) through solvothermal and low-temperature nitridation. Notably, the study finds for the first time that only Co LDH materials can be mostly converted to $CoN\text{-}N_d$ under the same nitriding conditions relative to different Co-based precursors. Experiments indicate that the constructed $CoN\text{-}N_d$ catalyst exhibits preeminent electrocatalytic activities for both oxygen evolution reaction (η_{10} = 243 mV) and oxygen reduction reaction (J_L = 5.2 mA cm^{-2}). Moreover, the $CoN\text{-}N_d$-based Zinc-air battery showed a large power density of 120 mW cm^{-2} and robust stability over 260 cycles, superior to the state-of-art Pt/C + RuO_2. The superior performance is attributed to a large number of defects formed by the disordered arrangement of local atoms on the catalyst that facilitate the formation of more active sites, and alternate array-like structures thereof improving electrolyte diffusion and gas emission.

* Corresponding authors.
E-mail addresses: chemdjx@gxnu.edu.cn (J. Dong), isimjant@sabic.com (T. Taylor Isimjan), xlyang@gxnu.edu.cn (X. Yang).

[1] Yan Hu and Man Guo equally contributed to this work.

https://doi.org/10.1016/j.jcis.2021.10.128
0021-9797/

1. Introduction

In recent years, electrochemical technologies have played a key role in searching for reusable energy sources, including water splitting, fuel cells, and metal-air batteries to drive the development of clean and sustainable energy storage and conversion [1,2]. Rechargeable Zinc-air batteries (ZAB) have been extensively studied due to their high theoretical energy density, low cost, and environmental friendliness [3,4]. It is essential to develop cost-effective and durable electrocatalysts with high ORR and OER electrocatalytic activities for advanced ZAB [3,5]. However, the slow kinetics of OER and ORR impede excessively high electric potentials and low energy efficiency: $O_2 + 2H_2O + 4e^- \leftrightarrow 4OH^-$ [6]. Currently, batch mark OER and ORR catalysts used for ZAB are based on precious metals (Pt, Ru, and Ir) that have high costs and scarcity greatly limiting their large-scale commercial applications [7,8]. Therefore, it is of great significance to develop non-noble metal-based bifunctional electrocatalysts with high efficiency and durability for Zn-air batteries.

At present, the main challenge in catalyst design is to achieve versatility while maintaining high bifunctional catalytic activity at a low cost [9,10]. Alternative non-precious metal bifunctional oxygen electrocatalysts have been developed as Zn air cathodes, including metal-free carbon matrix composites, transition metal oxides [11,12], sulfides [13,14], and phosphides [15,16]. Among these electrocatalysts, cobalt-based transition metal-nitrogen-carbon (Co—N—C) composites are preferred owing to their low cost, excellent activity, and good stability [17,18]. However, it is difficult to prepare well-defined metal-nitrogen co-doped carbon catalysts due to the aggregation of metal atoms at high temperatures during the synthesis [19,20] that places of interest in low-temperature synthesis. Nevertheless, synthesizing ORR catalysts with high activity at a mild temperature is often very challenging [11,21]. In addition, other cobalt-based materials, such as cobalt oxides [22,23], cobalt sulfides [13,24], and cobalt phosphides [15,25] also have been studied, but suffer from poor catalytic activity and stability attributable to the alkaline corrosion during battery operation. Therefore, fabricating a single function Co-based catalyst with an ORR or OER is a relatively easier process owning to the less complicity. Nevertheless, there are still a few reports on high-performance cobalt-based catalysts with dual-functionalities [26,27]. For instance, Yu et al [28] described Co nano-islands rooted on Co—N—C nano-sheets derived from electrodeposition with outstanding bifunctional property for ZAB. The ZAB showed a small charge–discharge voltage (0.82@10 mA cm^{-2}), high energy density (132 mW cm^{-2}), and outstanding durability. The DFT studies revealed that the synergy between Co metal particles and Co-N species is responsible for the high performance. However, it would be very difficult to keep the Co at the metallic state due to the very low oxidation potential. Especially when the Co is in the nano-form, the Co particles will be oxidized immediately in the air and it could cause a safety hazard, as the result the catalyst conductivity will be reduced so as the catalytic performance. In summary, catalyst aggregation and stability are the bottlenecks remaining unresolved in the field. Recent studies show that the cobalt nitride (Co_xN) possesses a unique advantage resulted from the Co-N bonding including better electron conductivity and good alkaline stability [29,30].

In the light of the above studies, we propose a novel strategy to synthesize a self-supporting CoN-N$_d$ nanosheet array on carbon cloth (CC) as a bifunctional oxygen electrocatalyst through a facile hydrothermal process and *in-situ* thermal nitridation treatment·NH_3 gas was used as a nitrogen source and annealed at a low temperature to ensure that the nanosheet structure of the catalyst remains intact during the post-annealing process. The activity of the catalyst was greatly promoted due to the high conversion of Co into CoN and the abounded N atom defect sites in the material. The optimized CoN-N$_d$-300 acts as an efficient bifunctional catalyst with high activity and outstanding durability toward both ORR and OER in alkaline solution (All potentials was calibrated to RHE, Fig. S1). The rechargeable ZAB using CoN-N$_d$ as an air cathode showed a small potential voltage (0.79@10 mA cm^{-2}), a high power density (120 mW cm^{-2}), and robust durability up to 260 cycles. This work provides guiding strategies for the construction of bifunctional electrocatalysts.

2. Experimental section

2.1. Materials

Cobalt(II) acetate tetrahydrate ($C_4H_6CoO_4·4H_2O$, 99.5%), Polyvinylpyrrolidone (PVP, K29, MW:58000), P_{123} (MW: 8400), F_{127} (MW: 12600), Ethylene glycol ($C_2H_6O_2$, AR), Methanol anhydrous (CH_3OH, AR 99.5%) were analytical reagent and used without further purification. Commercial Pt/C (20 wt% for platinum) was purchased from Alfa Aesar. RuO_2 powder is synthesized by directly calcining $RuCl_3$ in the air at 400 °C.

2.2. Synthesis of Co LDH/CC nanosheets

200 mg of Cobalt (II) acetate tetrahydrate and 400 mg of PVP were dissolved in 7.5 mL of ethylene glycol under stirring. Then, 22.5 mL of methanol was added to the above solution and under vigorous stirring for 0.5 h. A piece of carbon cloth (CC, 1 cm × 4 cm) was ultrasonically cleaned in 0.5 M H_2SO_4, deionized water, and ethanol for 15 min to remove impurities, respectively. Then the solution was transferred into a 50 mL Teflon-lined stainless steel autoclave containing the pretreated CC and kept at 120 °C for 12 h. After the autoclave cooled down slowly at room temperature, the resulting pink CC was taken out and further washed three times with ethanol and dried under vacuum at 60 °C.

For comparison, PVP was replaced with an equivalent amount of F_{127} or P_{123} during the synthesis process.

2.3. Synthesis of CoN/CC nanosheets

The obtained Co LDH/CC was placed in a tube furnace and annealed at 200 °C, 300 °C, and 400 °C for 3 h with a ramp rate of 5 °C min^{-1} under a flow of ammonia gas, respectively. The obtained sample was denoted as CoN/CC-200, CoN-N$_d$/CC-300, and CoN/CC-400, respectively. Note: N$_d$ denotes N defect.

2.4. Synthesis of CoN-CoCH

We use the previous synthesis method to synthesize CoCH, only replacing NF with carbon cloth (CC) [31]. The obtained sample is then annealed in an ammonia atmosphere of 300 °C using the same nitriding method described above.

2.5. Synthesis of ZIF 67-N_{300}

ZIF 67 was synthesized using previous laboratory synthesis methods [32]. Then the obtained sample is annealed in an ammonia atmosphere of 300 °C using the same nitriding method described above.

2.6. Zn-air battery fabrication

The homemade Zn-air battery was assembled according to the following process: the air electrode was made by loading catalyst ink onto the carbon paper substrate (loading: 1 mg cm^{-2}). The catalyst ink was prepared by mixing electrocatalysts with 5% Nafion solution and water/isopropanol solution (1:3 (v/v)). 6 M KOH and 0.2 M $Zn(Ac)_2$ were served as electrolytes. Then a polished zinc plate was used as the anode. As a comparison, Pt/C + RuO_2 mixed catalyst ink was prepared in the same procedure with a mass ratio of 1:1. All electrochemical tests were conducted on an electrochemical workstation (CHI 760E) under ambient conditions. The stability was tested by using the LAND battery testing system (BT2016A) at a current density of 5 mA cm^{-2} with 20 min per cycle (10 min charge and 10 min discharge). The specific capacity was calculated from the following equation:

$$\text{Specific capacity} = \frac{discharge\ current \times time}{weight\ of\ consumed\ Zinc}$$

3. Results and discussion

The synthetic processes of the CoN-N_d/CC are illustrated in Fig. 1a. The solvothermal method was used to prepare Co LDH nanosheet arrays grown in situ on carbon cloth (CC). Then, the precursor Co LDH is transformed into CoN-N_d nanosheets composed of nanoparticles by *in-situ* thermal ammonia treatment. The SEM image of Fig. 1b shows that a smooth CC surface before the *in-situ* growth of Co LDH species. After Co LDH is deposited, an interconnected sheet-like nanoarray is formed (Fig. 1c). After ammonia treatment at different temperatures, the morphologies of the Co_xN series are consistent with these of the Co LDH precursors (Fig. 1d and Fig. S2).. The abundant gaps between the array-like structures facilitate the transport and release of electrolytes and gases, thereby improving catalytic performance.

The precursors and the corresponding ammonia-treatment products at different temperatures were analyzed by X-ray diffraction (XRD). After heating the Co LDH/CC under NH_3 atmosphere at different temperatures (200–400 °C), The Co LDH nanosheets were converted to Co_xN nanosheets. However, there is a significant discrepancy in the crystal structure of the obtained Co_xN at the different annealing temperatures. Fig. 2a shows the XRD pattern of the Co LDH precursor, which shows that the precursor has high crystallinity. For comparison, Fig. 2b-d shows the XRD patterns of the ammonia-treatment products. In Fig. 2b, the diffraction peak located near 42.2° corresponds to the crystal plane of CoN (200), while the other diffraction peaks correspond to the (001), (003), (006), and (110) crystal planes of Co LDH, respectively. It shows that CoN-200 is not completely nitridated at a temperature of 200 °C. The diffraction peaks of the annealed sample at 300 °C are positioned at around 36.2, 42.2, 61.3, 73.3, and 76.8° corresponding to (111), (200), (220), (311), and (222) crystal planes of CoN (JCPDS: 16–0116), respectively [33,34]. Moreover, no diffraction peaks of precursors and impurities were observed, suggesting a complete phase conversion from precursor to CoN at 300 °C (Fig. 2c). The diffraction peaks in the sample revealed the coexistence of CoN and $Co_{5.47}N$ (JCPDS: 41–0943) in CoN-400 (Fig. 2d), after further annealing at 400 °C [35]. The above XRD analysis indicate that the crystal structure of Co_xN nanosheets can be adjusted by changing the annealing temperature, which provides an opportunity to evaluate the catalytic activities of Co_xN with different crystal phases.

Moreover, the influences of different surfactants on the CoN crystallinity and morphology were also investigated. As depicted in Fig. S3, the obtained Co LDH-s (s = PVP, F_{127}, P_{123}) and the series of CoN-s have similar crystal structures. However, there are palpable differences in the micromorphology of CoN-s (Fig. S4). SEM images show that CoN-P_{123} and CoN-F_{127} have granular and stacked sheet-shaped structures, respectively, while the interconnected sheet-like nanoarrays presented by CoN-PVP are more propitious to electrolyte diffusion and gas emission, thus contributing to better electrocatalytic activity (Fig. S5).

Besides, we further discussed the nitrogen treatment products of different cobalt-based precursors at 300 °C under an ammonia atmosphere. XRD patterns found that only some of the orthorhombic $Co(CO_3)_{0.5}(OH){\cdot}0{\cdot}11H_2O$ (CoCH) was converted to CoN, while the crystal structure of ZIF-67 material hardly changed (Figs. S6a-c). These results indicate that only Co LDH can be converted completely to CoN by treatment in an ammonia atmosphere at 300 °C, and shows better OER performance than other control materials (Fig. S6d). The study found that the differences in the morphology (Fig. S7), composition and crystal structure of CoN-CoCH and ZIF-67-N_{300} are the key factors maximizing the results of ammonia treatment.

Furthermore, the nitrogen adsorption–desorption isotherms of the series of CoN-N_d (Scraped off the CC) show a typical type-IV behavior (Fig. 2e). Among all samples, the CoN-N_d-300 nanosheets have the largest Brunauer–Emmett–Teller (BET) surface area (74.3 m^2 g^{-1}), which is higher than those of Co LDH (18.4 m^2 g^{-1}), CoN-200 (24.0 m^2 g^{-1}), and CoN-400 (24.3 m^2 g^{-1}) nanosheets. The average BJH pore diameters of Co LDH, CoN-200, CoN-N_d-300, and CoN-400 are 3.3, 3.9, 3.7, and 3.9 nm, respectively (Figs. S8a-c). This change may be due to the different crystalline forms of CoN at different ammonia-treatment temperatures, thus showing different porosity. The high porosity of CoN-N_d-300 facilitates the mass transfer and exposes more active sites, which greatly promotes electrocatalytic performance [36,37].

Electron paramagnetic resonance (EPR) spectra were employed to determine the formation of defects (Fig. 2f). A broad signal (*g* at 2.088) can be assigned to the contribution from unpaired electrons, indicating N defects exist in the CoN-N_d [31,38,39]. It can be found that the signal intensity of CoN-N_d-300 is significantly higher than those of Co LDH nanosheets, CoN-200 and CoN-400, indicating that the array-like CoN-N_d-300 has a higher degree of defects. The studies confirmed that the N defects create free electrons resulting in higher conductivity and additional active sites, thereby increasing the catalytic activity [38,40]. In addition, as shown in Fig. S9, the HRTEM image of CoN-N_d revealed many discontinuities presenting in the lattice fringes (marked with red dashed circles), indicating that there are abundant defects in CoN-N_d. These results indicate that the ammoniate temperature of 300 °C is the optimal condition for the formation of abundant nitrogen defects.

Transmission electron microscopy (TEM) is used to study the structural features of the CoN/CC. Fig. 3a shows that the CoN-N_d nanosheets are composed of nanoparticles with an average particle size of *ca.* 10 nm. The selected area electron diffraction (SAED) mode (Fig. 3b) shows the diffraction spots of CoN (111), (220) and (331) [40]. The HR-TEM image presents three types of lattice fringes (Fig. 3c), corresponding to the interplanar spacings of 0.248 nm (111), 0.151 nm (220), and 0.214 nm (200) of the cubic CoN crystal plane, respectively, corroborating the successful synthesis of CoN crystal [40]. Notably, the HRTEM images of CoN-N_d have many discontinuity points (marked by a white dotted circle), indicating the presence of a defect-rich structure on the base

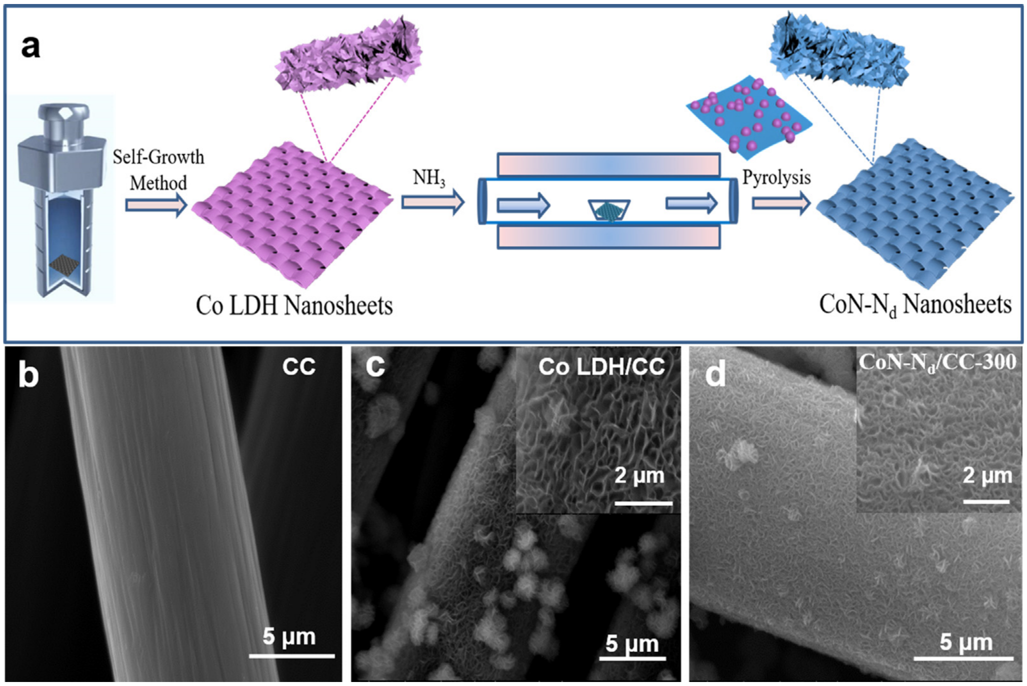

Fig. 1. (a) Schematic illustration of the synthesis of CoN-N_d/CC. (b-d) SEM images of CC, Co LDH/CC, and CoN-N_d/CC.

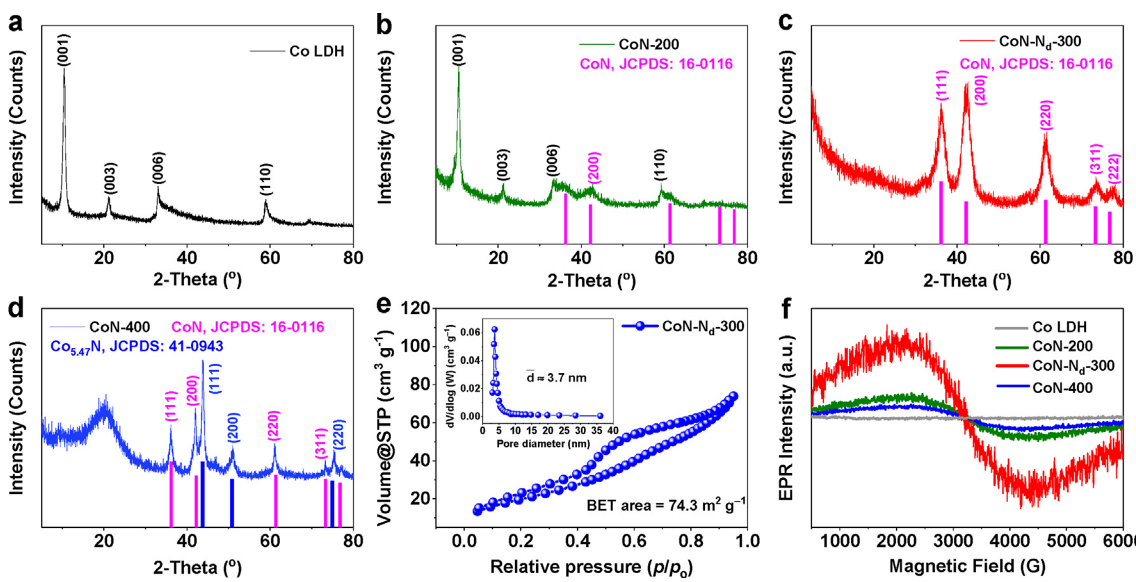

Fig. 2. (a-d) XRD of Co LDH, CoN-200, CoN-N_d-300, and CoN-400. (e) Nitrogen adsorption–desorption isotherms and the BJH pore-size distribution curves (inset) of CoN-N_d-300. (f) The ESR spectra of CoN-N_d-300 (peeled off from the CC).

surface. A locally disordered arrangement of atoms causes a large number of defects on the substrate, and thus amorphous structures are observed in the catalyst, which leads to the formation of the secondary active sites [38,39]. Meanwhile, the high-angle annular dark field (HAADF) TEM element mapping shows that Co and N are uniformly distributed throughout the CoN-N_d/CC (Fig. 3d), further demonstrating the CoN-N_d nanosheet formation.

X-ray photoelectron spectroscopy (XPS) was used to detect the chemical states of surface elements in CoN-x synthesized at different temperatures. The XPS survey spectrum reveals the presence of Co, N, C, and O elements in all samples (Fig. S10a). Three typical peaks at 284.0, 284.8, and 286.0 eV observed in C 1 *s* spectra are deconvoluted to C═C, C—C, and C—O as a calibration standard (Fig. S10b) [32,41]. By examining the hydrothermal sample as shown in Fig. S10c, the Co 2$p_{3/2}$ spectral deconvolution of Co LDH nanosheets can be performed as three components locating at 780.7, 782.2 and 786 eV, belonging to the Co^{3+}, Co^{2+}, and satellite peaks, respectively, which are consistent with two kinds of coordination environments of Co species in Co LDH [42,43]. Meanwhile, a weak single peak of pyrrolic-N was found in the high-resolution N 1 *s* of Co LDH due to a small number of PVP molecules adsorbed on the surface of the sample (Fig. S10d) [41].

The XPS results of Co and N elements in CoN-x (x = 200, 300, and 400) are shown in Fig. 4. All CoN-x samples observed the presence of Co^{3+}, Co^{2+}, and the corresponding satellites [44]. Notably,

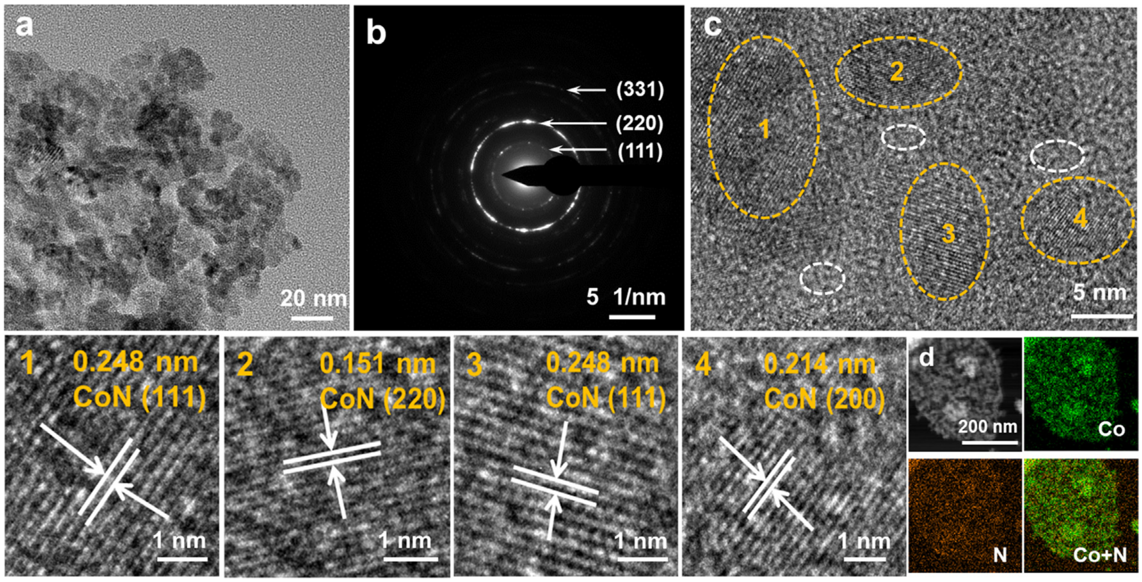

Fig. 3. (a) TEM image, (b) SAED and (c) High-Resolution TEM images, and (d) HAADF-STEM image and corresponding elemental mappings of CoN-N_d/CC (color online).

the peaks at 779.9 and 781.9 eV for Co $2p_{3/2}$ indicate the chemical features of Co^{3+} and Co^{2+}. Anecdotally, the percentage of Co^{3+} gradually increases with the rise of nitriding temperature (Fig. 4a). Fig. 4b illustrates the XPS spectrum of N 1 s for CoN-x. The high-resolution N 1 s spectrum of CoN-N_d-300 indicates that the peak of *N*-Co located at 398.2 eV was observed in addition to the N—H surface terminal group from NH_3 treatment [45,46]. Moreover, compared with CoN-200 and 400, when the nitriding temperature was 300 °C, the relative peak strength of Co-N was the strongest and the surface percentage was as high as 89.1%, indicating that the condition of 300 °C was most favorable for the formation of Co-N bond.

The OER behavior of the catalysts was measured by using a standard three-electrode system in 1.0 M KOH at a scan rate of 2 mV s^{-1}. Fig. 5a shows the current density of CoN-N_d-300 catalyst increases rapidly with potential, indicating the excellent OER performance. A significant effect of the *N*-defect was presented itself in OER performance, where the CoN-N_d-300 demands a lower overpotential of 243 mV to reach the current density of 10 mA cm^{-2}. It is much lower than these of Co LDH (243 mV), CoN-200 (291 mV), CoN-400 (310 mV), and RuO_2 (257 mV), and most recently reported electrocatalysts (Table S1). Another critical reaction of OER electrocatalytic activity is the small Tafel slope. As shown in Fig. 5b, the Tafel slope of 70.8 mV dec^{-1} for CoN-N_d-300 is smaller than those of Co LDH (74.6 mV dec^{-1}), CoN-200 (74.0 mV dec^{-1}), CoN-400 (75.8 mV dec^{-1}), and RuO_2 (73.3 mV dec^{-1}), suggesting faster reaction kinetics [32]. To further elucidate the intrinsic mechanism for the enhancement of OER activity, per-site turnover frequency (TOF) is employed to compare the practical performance of catalysts. The TOF value is calculated based on the assumption that all metal atoms are active sites, and the number of metal atoms is obtained by ICP-AES (Table S2) [47]. The potential-dependent TOF curve of CoN-N_d-300 catalyst shows the enhanced intrinsic activity per site compared to Co LDH, CoN-200, and CoN-400 (Fig. 5c). As expected, the CoN-N_d-300 catalyst possesses the largest electrochemically active surface area (ECSA) of 6208 cm^2 (normalized per cm^2 of electrode area), which is much higher than those of Co LDH (4386 cm^2), CoN-200 (4328 cm^2), and CoN-400 (1121 cm^2) (Table S3).

Electrochemical impedance spectroscopy (EIS) (Fig. 5d) shows that CoN-N_d-300 has the smallest charge transfer resistance (R_{ct}) than others, verifying that CoN-N_d-300 catalyst exhibits a faster electron transfer rate during the electrocatalytic OER process. Generally, the electrochemical double-layer capacity (C_{dl}) is directly proportional to the ECSA. The C_{dl} value can be calculated using cyclic voltammetry (CV) curves in the non-Faradaic region (Fig. S11) [48]. As shown in Fig. 5e, the C_{dl} values of CoN-N_d-300 is 372.5 mF cm^{-2}, which is significantly higher than those of Co LDH (263.2 mF cm^{-2}), CoN-200 (259.7 mF cm^{-2}), and CoN-400 (67.3 mF cm^{-2}), indicating more active sites in CoN-N_d/CC-300. Noticeably, using CoN-N_d/CC-300 as the working electrode, the durability of the catalyst was probed through constant current electrolysis at 100 mA cm^{-2} for 100 h (Fig. 5f). The stability of the catalyst deteriorates slightly over time, which may be caused by the change of the destruction of the microstructure (Fig. S12) and the surface chemical state (Fig. S13). Nevertheless, the CoN-N_d/CC-300 showed way better stability as compare to Pt/C (Fig. 6f).

The electrocatalytic performance of CoN-N_d for ORR was assessed by rotating disk electrode (RDE) and rotating ring disk electrode (RRDE) methods in 0.1 M KOH electrolyte. Fig. 6a depicted the CV curves of CoN and Pt/C in O_2 and N_2-saturated 0.1 M KOH solution. CoN showed a well-defined cathodic peak at about 0.78 V vs. RHE comparable to Pt/C, indicating the favorable ORR catalytic activity. The LSV curves and Tafel slopes of CoN-N_d and Pt/C were shown in Fig. 6b, c. The half-wave potential ($E_{1/2}$) of CoN-N_d (0.77 V) was only 0.07 V lower than that of Pt/C (0.84 V), while it's limit current density (J_L = 5.2 mA cm^{-2}) was 0.3 V higher than that of Pt/C (J_L = 4.9 mA cm^{-2}), and the Tafel slope was comparable to Pt/C [49]. Simultaneously, CoN-N_d showed a smaller charge transfer resistance compared to Pt/C (Fig. S14), illustrating CoN-N_d possesses a faster charge transfer rate [26]. The above results suggested that the robust ORR activity of CoN-N_d. To further understand the reaction mechanism, the LSV curves were recorded at different rotational speeds from 400 to 2025 rpm (Fig. S15a). The obtained Koutecky-Levich (K-L) diagram revealed an excellent linear relationship within the potential range of 0.3–0.6 V vs RHE, indicating that the number of electrons transferred per oxygen molecule was the same in the ORR process (Fig. S15b) [50]. Besides, the H_2O_2 yield of CoN was less than 15% and the electron transfer number (n) was ~4 in the potential range of 0.2–0.8 V, which further proves the four-electron process of ORR (Fig. 6d). The potential difference (ΔE) between $E_{1/2}$ of ORR and

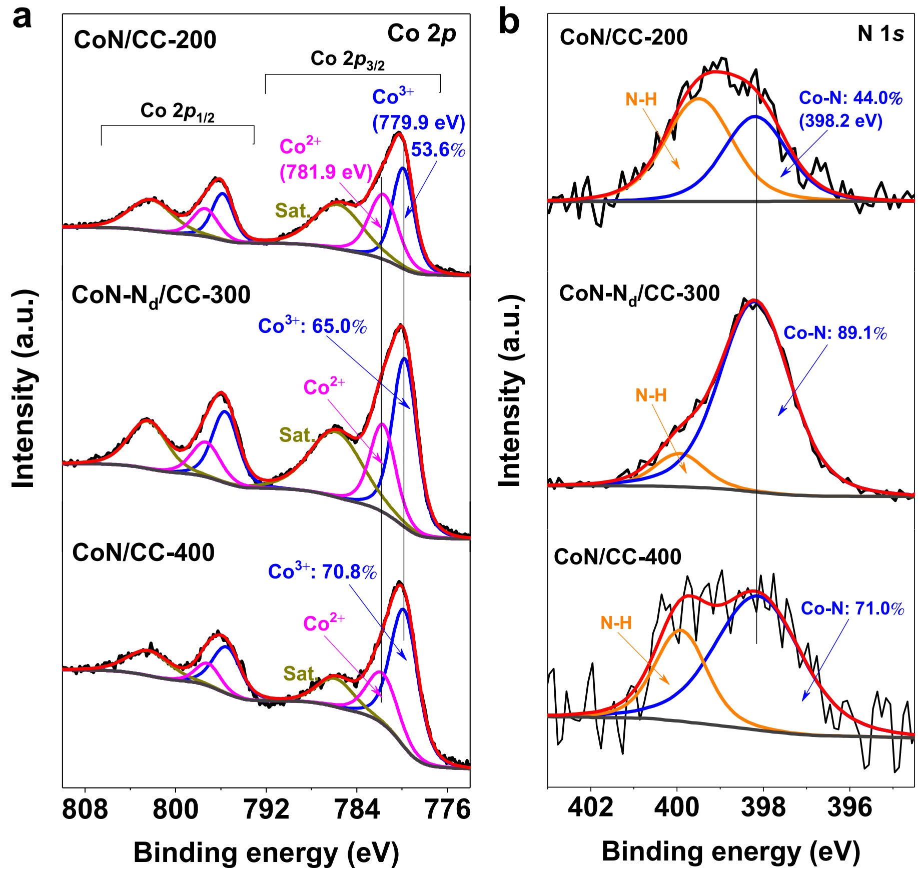

Fig. 4. XPS spectra of (a) Co 2p and (b) N 1 s regions from CoN/CC-200, CoN-N$_d$/CC-300 and CoN/CC-400, respectively.

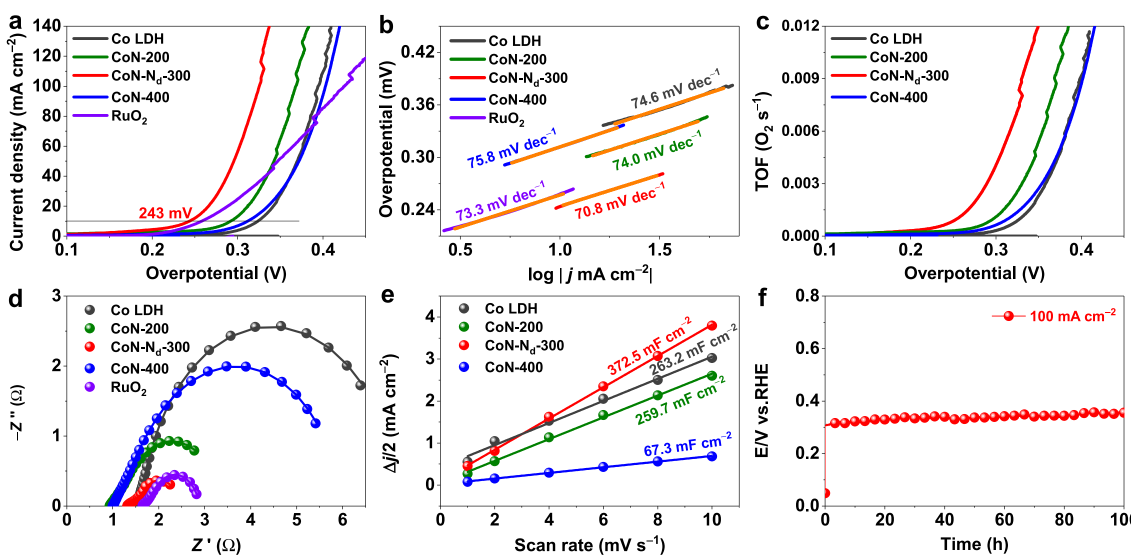

Fig. 5. Electrocatalytic OER performance. (a) LSV polarization curves, (b) corresponding Tafel slopes, (c) potential-dependent TOF curves, (d) electrochemical impedance spectroscopy (EIS), (e) summarized double-layer capacitance (C_{dl}) of Co LDH, CoN-200, CoN-N$_d$-300, CoN-400, and RuO_2 in 1.0 M KOH. (f) Durability test of CoN-N$_d$-300 at 100 mA cm^{-2} in 1.0 M KOH.

overpotential at 10 mA cm^{-2} (η_{10}) of OER was generally used to evaluate the overall bifunctional activity of the catalyst. The smaller ΔE value indicates the higher bifunctional activity [51]. As presented in Fig. 6e, the ΔE of CoN-N$_d$ (0.79 V) was equivalent to Pt/C + RuO_2 (0.78 V), which illustrates that CoN-N$_d$ possesses outstanding bifunctional activity. CV testing was performed in a mixed solution of 5 mM $K_3[Fe(CN)_6]$ and 0.1 M KCl with different scan rates to evaluate ECSA of CoN-N$_d$. As shown in Fig. S16, there is a good linear relationship between the peak current and scan rate, which indicates that CoN-N$_d$ has a large ECSA [52,53]. SCN^- was used as a probe to verify the role of CoN-N$_d$ during ORR because SCN^- poison the M–N$_x$ site [53]. The current density of

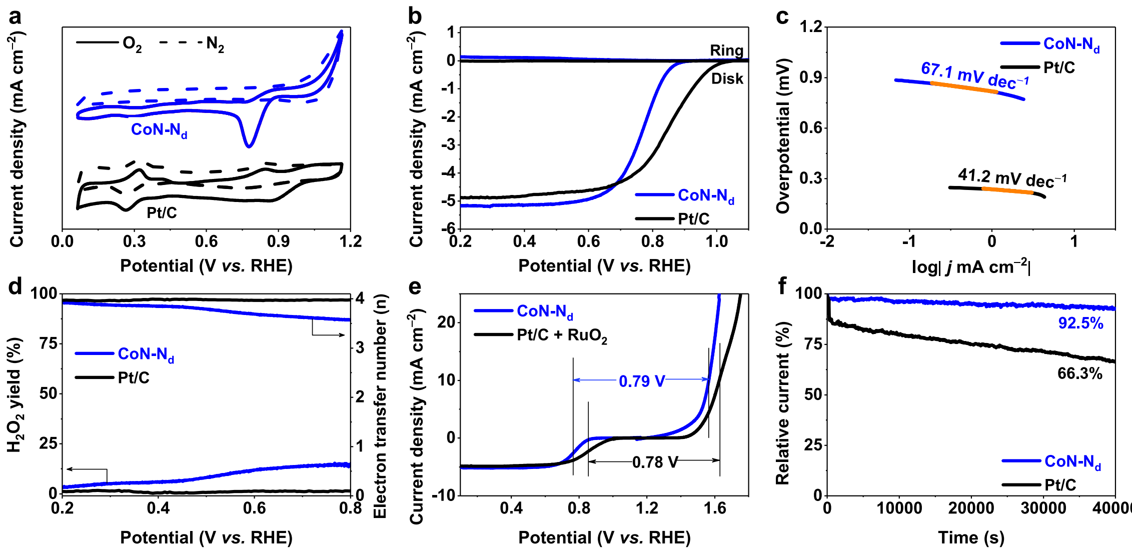

Fig. 6. Electrocatalytic ORR performance. (a) CV curves in O_2/N_2-saturated 0.1 M KOH electrolyte, (b) LSV polarization curves in O_2-saturated 0.1 M KOH with a rotation of 1600 rpm, (c) corresponding Tafel slopes, and (d) the H_2O_2 yield and electron transfer numbers (n) of CoN-N_d and Pt/C. (e) LSV polarization curves of CoN-N_d, Pt/C, and RuO_2 in the ORR-OER potential range in 0.1 M KOH. (f) Chronoamperometric response of CoN-N_d and Pt/C in O_2-saturated 0.1 M KOH solution.

CoN-N_d was decreased by 0.7 mA cm^{-2} after introducing SCN^-, proving that Co-N was the active site (Fig. S17a). Furthermore, the tolerance of methanol and long-term stability were also the important index for evaluating catalysts. There is no manifest current decay for CoN-N_d after the addition of 3 M CH_3OH about 200 s, while Pt/C display a significant degradation (Fig. S17b). The current of CoN-N_d was only reduced by 4.0% after 40000 s test, whereas the Pt/C suffer from decreased significantly by 36% (Fig. 6f). As expected, CoN-N_d exhibited superior methanol tolerance and stability. The outstanding electrocatalytic activity was attributed to the fact that the defect sites generated by the disordered arrangement of atoms on the catalyst can provide more active sites, higher conductivity accelerates electron transport, and the array-like structure promotes electrolyte diffusion and gas emission.

The rechargeable ZAB was assembled with CoN-N_d as the air cathode to evaluate the feasibility of the catalyst in practical applications, the schematic diagram as described in Fig. 7a. For comparison, Pt/C + RuO_2-based ZAB was tested under the same conditions. The charge and discharge performance of CoN-N_d as an air cathode were comparable to that of Pt/C + RuO_2 (Fig. 7b), following the ΔE result. Besides, the CoN-N_d-based ZAB achieves a power density of 120 mW cm^{-2}, which exceeds the Pt/C (100 mW cm^{-2}) (Fig. 7c). As depicted in Fig. 7d and e, the open-circuit voltage (OCV) of CoN-N_d-based ZAB (1.44 V) are comparable to Pt/C + RuO_2 (1.48 V) and the LED can be lit by two ZAB in series. Noticeably, the specific capacity of ZAB based on CoN-N_d, which is equivalent to Pt/C + RuO_2 (711 mAh g^{-1}), was calculated to be 702 mAh g^{-1} based on the normalized zinc consumption (Fig. 7e). Meanwhile, the rate performance was evaluated under different current densities. As shown in Fig. S18, a stable platform was shown at various current densities, indicating that CoN-N_d-based ZAB has a good rate performance. The cyclic stability was a vital parameter to investigate the

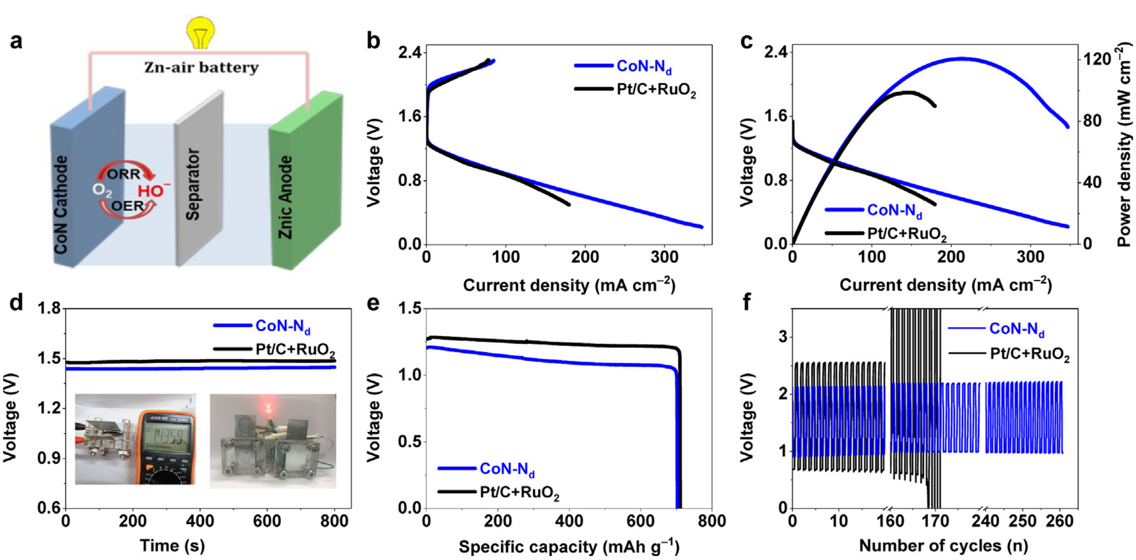

Fig. 7. (a) The configuration of the homemade Zn-air battery. (b) The charge–discharge curves, and (c) polarization curves, and corresponding power density of CoN-N_d and Pt/C + RuO_2. (d) The open-circuit potential of Zn-air battery (Inset: a photograph of a Zn-air battery showing an open-circuit voltage and another photograph of LED powered by two Zn-air batteries in series). (e) The galvanostatic discharge curve at 10 mA cm^{-2}, and (f) long-term cycling stability at a current density of 10 mA cm^{-2}.

practical application of ZAB. As illustrated in Fig. 7f, the CoN-N_d-based ZAB displayed superior cycling stability about 260 cycles with loss of discharge voltage was hardly observed, demonstrating it exhibited outstanding stability. In contrast, ZAB based on Pt/C + RuO_2 emerged a remarkable decline after 150 cycles. The above results prove that CoN-N_d is a promising electrocatalyst for metal-air battery application.

The abundant *N*-defect sites in the CoN-N_d sheet-like array catalyst are beneficial to enhance the adsorption capacity of OH^- and reduce the Gibbs free energy of the reaction intermediate, thus improving the catalytic activity of OER. Many studies have confirmed that the Co-N active sites play a key role in ORR activity [20,54]. Typically, the synergy between the *N*-deficient Co-N active site and the carbon black mixture can not only improve the electron transport efficiency but also reduce the reaction energy barrier of the active site, thereby increasing the ORR activity [54-56].

4. Conclusion

In summary, we have successfully synthesized highly efficient bifunctional CoN-N_d electrocatalysts using a simple and scalable low-temperature pyrolysis approach. This study is the first to observe that only Co LDH materials can be fully converted to CoN-N_d compared to other Co-based precursors under the same nitridation conditions. TEM and EPR affirmed the presence of abundant N defect sites in CoN-N_d at the pyrolysis temperature of 300 °C. SEM confirmed that the use of surfactants gave rise to differences in morphology and catalytic activity of CoN-N_d. More importantly, the as-prepared CoN-N_d sheet-like array catalyst indicated superb OER and ORR performances in alkaline media. The results are comparable to most of the recently reported transition metal catalysts. Besides, the Zinc-air batteries assembled with CoN-N_d as the air cathode achieved a high peak power density of 120 mW cm^{-2} and outstanding stability. The excellent performance is attributed to the unique structure providing abundant active sites, faster charge transfer rate, electrolyte diffusion rate, and gas release. This work provides a facile strategy of constructing nitrogen defects rich bifunctional-electrocatalysts and proves its promising application prospects in metal-air batteries.

CRediT authorship contribution statement

Yan Hu: Writing – original draft, Conceptualization, Investigation. **Man Guo:** Writing – original draft, Conceptualization, Investigation. **Chuan Hu:** Formal analysis, Methodology. **Jiaxin Dong:** Data curation, Software. **Puxuan Yan:** Formal analysis, Investigation. **Tayirjan Taylor Isimjan:** Writing – review & editing. **Xiulin Yang:** Writing – review & editing, Supervision.

Declaration of Competing Interest

The authors declare that they have no known competing financial interests or personal relationships that could have appeared to influence the work reported in this paper.

Acknowledgments

This work has been supported by the National Natural Science Foundation of China (no. 21965005), Natural Science Foundation of Guangxi Province (2018GXNSFAA294077, 2021GXNSFAA076001), Project of High-Level Talents of Guangxi (F-KA18015), and Guangxi Technology Base and Talent Subject (GUIKE AD18126001, GUIKE AD20297039).

Appendix A. Supplementary material

Supplementary data to this article can be found online at https://doi.org/10.1016/j.jcis.2021.10.128.

References

[1] Z. Kou, W. Zang, Y. Ma, Z. Pan, S. Mu, X. Gao, B. Tang, M. Xiong, X. Zhao, A.K. Cheetham, L. Zheng, J. Wang, Cage-confinement pyrolysis route to size-controlled molybdenum-based oxygen electrode catalysts: From isolated atoms to clusters and nanoparticles, Nano Energy 67 (2020) 104288.

[2] Z. Kou, X. Li, L. Zhang, W. Zang, X. Gao, J. Wang, Dynamic surface chemistry of catalysts in oxygen evolution reaction, Small Science 1 (2021) 2100011.

[3] D. Chen, J. Zhu, X. Mu, R. Cheng, W. Li, S. Liu, Z. Pu, C. Lin, S. Mu, Nitrogen-Doped carbon coupled $FeNi_3$ intermetallic compound as advanced bifunctional electrocatalyst for OER, ORR and zn-air batteries, Appl. Catal. B: Environ. 268 (2020) 118729.

[4] H. Zou, G. Li, L. Duan, Z. Kou, J. Wang, In situ coupled amorphous cobalt nitride with nitrogen-doped graphene aerogel as a trifunctional electrocatalyst towards Zn-air battery deriven full water splitting, Appl. Catal. B: Environ. 259 (2019) 118100.

[5] T. Ling, D.Y. Yan, Y. Jiao, H. Wang, Y. Zheng, X. Zheng, J. Mao, X.W. Du, Z. Hu, M. Jaroniec, S.Z. Qiao, Engineering surface atomic structure of single-crystal cobalt (II) oxide nanorods for superior electrocatalysis, Nat. Commun. 7 (2016) 12876.

[6] S. Liu, C. Sun, J. Chen, J. Xiao, J.-L. Luo, A High-Performance Ruddlesden-Popper Perovskite for Bifunctional Oxygen Electrocatalysis, ACS Catal. 10 (22) (2020) 13437–13444.

[7] Z. Wang, B. Xiao, Z. Lin, S. Shen, A. Xu, Z. Du, Y. Chen, W. Zhong, In-situ surface decoration of RuO_2 nanoparticles by laser ablation for improved oxygen evolution reaction activity in both acid and alkali solutions, J. Energy Chem. 54 (2021) 510–518.

[8] L. Zhang, T. Yang, W. Zang, Z. Kou, Y. Ma, M. Waqar, X. Liu, L. Zheng, S.J. Pennycook, Z. Liu, X.J. Loh, L. Shen, J. Wang, Quasi-Paired Pt Atomic Sites on Mo_2C Promoting Selective Four-Electron Oxygen Reduction, Adv. Sci. 8 (2021) 2101344.

[9] Y. Tan, W. Zhu, Z. Zhang, W. Wu, R. Chen, S. Mu, H. Lv, N. Cheng, Electronic tuning of confined sub-nanometer cobalt oxide clusters boosting oxygen catalysis and rechargeable Zn–air batteries, Nano Energy 83 (2021) 105813.

[10] F. Yang, X. Liu, H. Zhang, J. Zhou, J. Jiang, X. Lu, Boosting oxygen catalytic kinetics of carbon nanotubes by oxygen-induced electron density modulation for advanced Zn-Air batteries, Energy Storage Mater. 30 (2020) 138–145.

[11] J. Yin, Y. Li, F. Lv, Q. Fan, Y.-Q. Zhao, Q. Zhang, W. Wang, F. Cheng, P. Xi, S. Guo, NiO/CoN Porous Nanowires as Efficient Bifunctional Catalysts for Zn-Air Batteries, ACS Nano 11 (2) (2017) 2275–2283.

[12] N.-F. Yu, C. Wu, W. Huang, Y.-H. Chen, D.-Q. Ruan, K.-L. Bao, H. Chen, Y. Zhang, Y. Zhu, Q.-H. Huang, W.-H. Lai, Y.-X. Wang, H.-G. Liao, S.-G. Sun, Y.-P. Wu, J. Wang, Highly efficient Co_3O_4/Co@NCs bifunctional oxygen electrocatalysts for long life rechargeable Zn-air batteries, Nano Energy 77 (2020) 105200.

[13] C. Cao, D.-D. Ma, J.-F. Gu, X. Xie, G. Zeng, X. Li, S.-G. Han, Q.-L. Zhu, X.-T. Wu, Q. Xu, Metal–organic Layers Derived Atomically Thin Bismuthene for Efficient Carbon Dioxide Electroreduction to Liquid Fuel, Angew. Chem. Int. Ed. 59 (2020) 15014–15020.

[14] D.C. Nguyen, D.T. Tran, T.L.L. Doan, D.H. Kim, N.H. Kim, J.H. Lee, Rational Design of Core@shell Structured CoS_x@Cu_2MoS_4 Hybridized MoS_2/N, S-Codoped Graphene as Advanced Electrocatalyst for Water Splitting and Zn-Air Battery, Adv. Energy Mater. 10 (2020) 1903289.

[15] Y. Wang, M. Wu, J. Li, H. Huang, J. Qiao, In situ growth of CoP nanoparticles anchored on (N, P) co-doped porous carbon engineered by MOFs as advanced bifunctional oxygen catalyst for rechargeable Zn–air battery, J. Mater. Chem. A 8 (36) (2020) 19043–19049.

[16] S. Dresp, T. Ngo Thanh, M. Klingenhof, S. Brückner, P. Hauke, P. Strasser, Efficient direct seawater electrolysers using selective alkaline NiFe-LDH as OER catalyst in asymmetric electrolyte feeds, Energy Environ. Sci. 13 (6) (2020) 1725–1729.

[17] J. Qin, Z. Liu, D. Wu, J. Yang, Optimizing the electronic structure of cobalt via synergized oxygen vacancy and Co-N-C to boost reversible oxygen electrocatalysis for rechargeable Zn-air batteries, Appl. Catal. B: Environ. 278 (2020) 119300.

[18] L. Chen, X. Liu, L. Zheng, Y. Li, X. Guo, X. Wan, Q. Liu, J. Shang, J. Shui, Insights into the role of active site density in the fuel cell performance of Co-N-C catalysts, Appl. Catal. B: Environ. 256 (2019) 117849.

[19] I.S. Amiinu, X. Liu, Z. Pu, W. Li, Q. Li, J. Zhang, H. Tang, H. Zhang, S. Mu, From 3D ZIF Nanocrystals to Co-N_x/C Nanorod Array Electrocatalysts for ORR, OER, and Zn-Air Batteries, Adv. Funct. Mater. 28 (2018) 1704638.

[20] E.A. Larson, J. Lee, A. Paulson, Y.J. Lee, Structural Analysis of Polyurethane Monomers by Pyrolysis GC TOFMS via Dopant-Assisted Atmospheric Pressure Chemical Ionization, J. Am. Soc. Mass Spectrom. 30 (6) (2019) 1046–1058.

[21] S.G. Chandrappa, P. Moni, D. Chen, G. Karkera, K.R. Prakasha, R.A. Caruso, A.S. Prakash, The influence of ruthenium substitution in $LaCoO_3$ towards bi-functional electrocatalytic activity for rechargeable Zn–air batteries, J. Mater. Chem. A 8 (39) (2020) 20612–20620.

[22] Q. Lu, Y. Guo, P. Mao, K. Liao, X. Zou, J. Dai, P. Tan, R. Ran, W. Zhou, M. Ni, Z. Shao, Rich atomic interfaces between sub-1 nm RuO_x clusters and porous

Co_3O_4 nanosheets boost oxygen electrocatalysis bifunctionality for advanced Zn-air batteries, Energy Storage Mater. 32 (2020) 20–29.
[23] D. Ding, K. Shen, X. Chen, H. Chen, J. Chen, T. Fan, R. Wu, Y. Li, Multi-Level Architecture Optimization of MOF-Templated Co-Based Nanoparticles Embedded in Hollow N-Doped Carbon Polyhedra for Efficient OER and ORR, ACS Catal. 8 (9) (2018) 7879–7888.
[24] J. Yin, Y. Li, F. Lv, M. Lu, K. Sun, W. Wang, L. Wang, F. Cheng, Y. Li, P. Xi, S. Guo, Oxygen Vacancies Dominated NiS_2/CoS_2 Interface Porous Nanowires for Portable Zn-Air Batteries Driven Water Splitting Devices, Adv. Mater. 29 (2017) 1704681.
[25] Y. Guo, P. Yuan, J. Zhang, H. Xia, F. Cheng, M. Zhou, J. Li, Y. Qiao, S. Mu, Q. Xu, Co_2P-CoN Double Active Centers Confined in N-Doped Carbon Nanotube: Heterostructural Engineering for Trifunctional Catalysis toward HER, ORR, OER, and Zn-Air Batteries Driven Water Splitting, Adv. Funct. Mater. 28 (2018) 1805641.
[26] J. Zhu, J. Fan, T. Cheng, M. Cao, Z. Sun, R. Zhou, L. Huang, D. Wang, Y. Li, Y. Wu, Bilayer nanosheets of unusual stoichiometric bismuth oxychloride for potassium ion storage and CO_2 reduction, Nano Energy 75 (2020) 104939.
[27] W. Zhu, L. Zhang, S. Liu, A. Li, X. Yuan, C. Hu, G. Zhang, W. Deng, K. Zang, J. Luo, Y. Zhu, M. Gu, Z.-J. Zhao, J. Gong, Enhanced CO_2 Electroreduction on Neighboring Zn/Co Monomers by Electronic Effect, Angew. Chem. Int. Ed. 59 (31) (2020) 12664–12668.
[28] P. Yu, L. Wang, F. Sun, Y. Xie, X. Liu, J. Ma, X. Wang, C. Tian, J. Li, H. Fu, Co Nanoislands Rooted on Co–N–C Nanosheets as Efficient Oxygen Electrocatalyst for Zn–Air Batteries, Adv. Mater. 31 (2019) 1901666.
[29] F. Xie, X. Cao, F. Qu, A.M. Asiri, X. Sun, Cobalt nitride nanowire array as an efficient electrochemical sensor for glucose and H_2O_2 detection, Sensor. Actuat. B-Chem. 255 (2018) 1254–1261.
[30] F. Meng, H. Zhong, D.i. Bao, J. Yan, X. Zhang, In Situ Coupling of Strung Co_4N and Intertwined N-C Fibers toward Free-Standing Bifunctional Cathode for Robust, Efficient, and Flexible Zn-Air Batteries, J. Am. Chem. Soc. 138 (32) (2016) 10226–10231.
[31] X. Huang, X. Xu, X. Luan, D. Cheng, CoP nanowires coupled with CoMoP nanosheets as a highly efficient cooperative catalyst for hydrogen evolution reaction, Nano Energy 68 (2020) 104332.
[32] P. Yan, M. Huang, B. Wang, Z. Wan, M. Qian, H.u. Yan, T.T. Isimjan, J. Tian, X. Yang, Oxygen defect-rich double-layer hierarchical porous Co_3O_4 arrays as high-efficient oxygen evolution catalyst for overall water splitting, J. Energy Chem. 47 (2020) 299–306.
[33] L. Hu, Y. Hu, R. Liu, Y. Mao, M.-S. Balogun, Y. Tong, Co-based MOF-derived Co/CoN/Co_2P ternary composite embedded in N- and P-doped carbon as bifunctional nanocatalysts for efficient overall water splitting, Int. J. Hydrogen Energy 44 (23) (2019) 11402–11410.
[34] C. Ray, S.C. Lee, B. Jin, A. Kundu, J.H. Park, S. Chan Jun, Chan Jun, Conceptual design of three-dimensional CoN/Ni_3N-coupled nanograsses integrated on N-doped carbon to serve as efficient and robust water splitting electrocatalysts, J. Mater. Chem. A 6 (10) (2018) 4466–4476.
[35] Z. Chen, Y. Ha, Y. Liu, H. Wang, H. Yang, H. Xu, Y. Li, R. Wu, In Situ Formation of Cobalt Nitrides/Graphitic Carbon Composites as Efficient Bifunctional Electrocatalysts for Overall Water Splitting, ACS Appl. Mater. Interfaces 10 (8) (2018) 7134–7144.
[36] P. Karfa, K.C. Majhi, R. Madhuri, Shape-Dependent Electrocatalytic Activity of Iridium Oxide Decorated Erbium Pyrosilicate toward the Hydrogen Evolution Reaction over the Entire pH Range, ACS Catal. 8 (9) (2018) 8830–8843.
[37] T. Zhou, H. Shan, H. Yu, C. Zhong, J. Ge, N. Zhang, W. Chu, W. Yan, Q. Xu, H. Wu, C. Wu, Y. Xie, Nanopore Confinement of Electrocatalysts Optimizing Triple Transport for an Ultrahigh-Power-Density Zinc-Air Fuel Cell with Robust Stability, Adv. Mater. 32 (47) (2020) 2003251, https://doi.org/10.1002/adma.202003251.
[38] Z. Zhang, J. Hao, W. Yang, J. Tang, Defect-Rich CoP/Nitrogen-Doped Carbon Composites Derived from a Metal-Organic Framework: High-Performance Electrocatalysts for the Hydrogen Evolution Reaction, ChemCatChem 7 (2015) 1920–1925.
[39] N.Q. Tran, B.K. Kang, M.H. Woo, D.H. Yoon, Enrichment of Pyrrolic Nitrogen by Hole Defects in Nitrogen and Sulfur Co-Doped Graphene Hydrogel for Flexible Supercapacitors, ChemSusChem 9 (16) (2016) 2261–2268.
[40] Z. Xue, J. Kang, D. Guo, C. Zhu, C. Li, X. Zhang, Y. Chen, Self-supported cobalt nitride porous nanowire arrays as bifunctional electrocatalyst for overall water splitting, Electrochim. Acta 273 (2018) 229–238.
[41] H. Zhang, D.J. Hagen, X. Li, A. Graff, F. Heyroth, B. Fuhrmann, I. Kostanovskiy, S. L. Schweizer, F. Caddeo, A.W. Maijenburg, S. Parkin, R.B. Wehrspohn, Atomic Layer Deposition of Cobalt Phosphide for Efficient Water Splitting, Angew. Chem. Int. Ed. 59 (39) (2020) 17172–17176.
[42] Q. Chen, R. Ding, H. Liu, L. Zhou, Y.i. Wang, Y. Zhang, G. Fan, Flexible Active-Site Engineering of Monometallic Co-Layered Double Hydroxides for Achieving High-Performance Bifunctional Electrocatalyst toward Oxygen Evolution and H_2O_2 Reduction, ACS Appl. Mater. Interfaces 12 (11) (2020) 12919–12929.
[43] Y. Lin, H. Wang, C.-K. Peng, L. Bu, C.-L. Chiang, K. Tian, Y. Zhao, J. Zhao, Y.-G. Lin, J.-M. Lee, L. Gao, Co-Induced Electronic Optimization of Hierarchical NiFe LDH for Oxygen Evolution, Small 16 (38) (2020) 2002426, https://doi.org/10.1002/smll.202002426.
[44] F. Song, W. Li, J. Yang, G. Han, T. Yan, X.i. Liu, Y.i. Rao, P. Liao, Z. Cao, Y. Sun, Interfacial Sites between Cobalt Nitride and Cobalt Act as Bifunctional Catalysts for Hydrogen Electrochemistry, ACS Energy Lett. 4 (7) (2019) 1594–1601.
[45] Y. Yang, R. Zeng, Y. Xiong, F.J. DiSalvo, H.D. Abruña, Cobalt-Based Nitride-Core Oxide-Shell Oxygen Reduction Electrocatalysts, J. Am. Chem. Soc. 141 (49) (2019) 19241–19245.
[46] R.-Q. Li, X.-Y. Wan, B.-L. Chen, R.-Y. Cao, Q.-H. Ji, J. Deng, K.-G. Qu, X.-B. Wang, Y.-C. Zhu, Hierarchical $Ni_3N/Ni_{0.2}Mo_{0.8}N$ heterostructure nanorods arrays as efficient electrocatalysts for overall water and urea electrolysis, Chem. Eng. J. 409 (2021) 128240.
[47] B. Wang, H. Huang, M. Huang, P. Yan, T.T. Isimjan, X. Yang, Electron-transfer enhanced MoO_2-Ni heterostructures as a highly efficient pH-universal catalyst for hydrogen evolution, Sci. China Chem. 63 (6) (2020) 841–849.
[48] B. Wang, H. Huang, T. Sun, P. Yan, T.T. Isimjan, J. Tian, X. Yang, Dissolution reconstruction of electron-transfer enhanced hierarchical NiS_x-MoO_2 nanosponges as a promising industrialized hydrogen evolution catalyst beyond Pt/C, J. Colloid Interface Sci. 567 (2020) 339–346.
[49] A.I. Douka, Y. Xu, H. Yang, S. Zaman, Y. Yan, H. Liu, M.A. Salam, B.Y. Xia, A Zeolitic-Imidazole Frameworks-Derived Interconnected Macroporous Carbon Matrix for Efficient Oxygen Electrocatalysis in Rechargeable Zinc-Air Batteries, Adv. Mater. 32 (2020) 2002170.
[50] X. Cheng, S. Dou, G. Qin, B. Wang, P. Yan, T.T. Isimjan, X. Yang, Rational design of highly selective nitrogen-doped Fe_2O_3-CNTs catalyst towards H_2O_2 generation in alkaline media, Int. J. Hydrogen Energy 45 (11) (2020) 6128–6137.
[51] Y. Niu, X. Teng, S. Gong, Z. Chen, A bimetallic alloy anchored on biomass-derived porous N-doped carbon fibers as a self-supporting bifunctional oxygen electrocatalyst for flexible Zn–air batteries, J. Mater. Chem. A 8 (27) (2020) 13725–13734.
[52] M. Qian, X. Cheng, T. Sun, J. Tian, T.T. Isimjan, Z. Shi, X. Yang, Synergistic catalytic effect of N-doped carbon embedded with CoFe-rich $CoFe_2O_4$ clusters as highly efficient catalyst towards oxygen reduction, J. Alloy. Compd. 819 (2020) 153015.
[53] M. Qian, M. Xu, S. Zhou, J. Tian, T. Taylor Isimjan, Z. Shi, X. Yang, Template synthesis of two-dimensional ternary nickel-cobalt-nitrogen co-doped porous carbon film: Promoting the conductivity and more active sites for oxygen reduction, J. Colloid Interface Sci. 564 (2020) 276–285.
[54] Y.-J. Wu, X.-H. Wu, T.-X. Tu, P.-F. Zhang, J.-T. Li, Y. Zhou, L. Huang, S.-G. Sun, Controlled synthesis of FeN_x-CoN_x dual active sites interfaced with metallic Co nanoparticles as bifunctional oxygen electrocatalysts for rechargeable Zn-air batteries, Appl. Catal. B: Environ. 278 (2020) 119259.
[55] S. Ramakrishnan, J. Balamurugan, M. Vinothkannan, A.R. Kim, S. Sengodan, D.J. Yoo, Nitrogen-doped graphene encapsulated FeCoMoS nanoparticles as advanced trifunctional catalyst for water splitting devices and zinc–air batteries, Appl. Catal. B: Environ. 279 (2020) 119381.
[56] Z. Zhang, X. Zhao, S. Xi, L. Zhang, Z. Chen, Z. Zeng, M. Huang, H. Yang, B. Liu, S.J. Pennycook, P. Chen, Atomically Dispersed Cobalt Trifunctional Electrocatalysts with Tailored Coordination Environment for Flexible Rechargeable Zn–Air Battery and Self-Driven Water Splitting, Adv. Energy Mater. 10 (2020) 2002896.